Monthly Notices
of the
ROYAL ASTRONOMICAL SOCIETY

MNRAS **492,** 5607–5619 (2020)
Advance Access publication 2020 January 21

doi:10.1093/mnras/staa164

NuSTAR and *Parkes* observations of the transitional millisecond pulsar binary XSS J12270–4859 in the rotation-powered state

D. de Martino [1]★ A. Papitto [2] M. Burgay [3] A. Possenti [3] F. Coti Zelati [4] N. Rea [4] D. F. Torres [4,5,6] and T. M. Belloni [7]

[1] *INAF – Osservatorio Astronomico di Capodimonte, Salita Moiariello 16, I-80131 Napoli, Italy*
[2] *INAF – Osservatorio Astronomico di Roma, via Frascati 33, I-00076 Monteporzio Catone (RM), Italy*
[3] *INAF – Osservatorio Astronomico di Cagliari, Via della Scienza, I-09047 Serlagius (CA), Italy*
[4] *Institució Catalana de Recerca i Estudis Avançats (ICREA), E-08010 Barcelona, Spain*
[5] *Institute of Space Sciences (ICE, CSIC), Campus UAB, Carrer de Can Magrans, E-08193 Barcelona, Spain*
[6] *Institut d'Estudis Espacials de Catalunya (IEEC), E-08034 Barcelona, Spain*
[7] *INAF – Osservatorio Astronomico di Brera, Via E. Bianchi 46, I-23807 Merate (LC), Italy*

Accepted 2020 January 15. Received 2019 December 16; in original form 2019 October 31

ABSTRACT

We report on the first *NuSTAR* observation of the transitional millisecond pulsar binary XSS J12270–4859 during its current rotation-powered state, complemented with a 2.5 yr-long radio monitoring at *Parkes* telescope and archival *XMM–Newton* and *Swift* X-ray and optical data. The radio pulsar is mainly detected at 1.4 GHz displaying eclipses over ~ 40 per cent of the 6.91 h orbital cycle. We derive a new updated radio ephemeris to study the 3–79 keV light curve that displays a significant orbital modulation with fractional amplitude of 28 ± 3 per cent, a structured maximum centred at the inferior conjunction of the pulsar and no cycle-to-cycle or low–high-flaring mode variabilities. The average X-ray spectrum, extending up to $\sim$70 keV without a spectral break, is well described by a simple power law with photon index $\Gamma = 1.17 \pm 0.08$ giving a 3–79 keV luminosity of $7.6^{+3.8}_{-0.8} \times 10^{32}$ erg s^{-1} for a distance of $1.37^{+0.69}_{-0.15}$ kpc. Energy resolved orbital light curves reveal that the modulation is not energy dependent from 3 to 25 keV and is undetected with an upper limit of $\sim$10 per cent above 25 keV. Comparison with previous X-ray *XMM–Newton* observations in common energy ranges confirms that the modulation amplitudes vary on time-scales of a few months, indicative of a non-stationary contribution of the intrabinary shock (IBS) formed by the colliding winds of the pulsar and the companion. A more detailed inspection of energy resolved modulations than previously reported gives hints of a mild softening at superior conjunction of the pulsar below 3 keV, likely due to the contribution of the thermal emission from the neutron star. The IBS emission, if extending into the MeV range, would be energetically capable alone to irradiate the donor star.

Key words: binaries: close – stars: individual: XSS J12270−4859 (aka 1FGL J1227.9−4852, 2FGL J1227.7−4853, 3FGL J1227.9−4854, PSR J1227−4853) – pulsars: general – gamma-rays: stars – X-rays: binaries.

1 INTRODUCTION

Millisecond pulsars (MSPs) are old neutron stars (NSs) in close binary systems which were spun-up to very short periods during a previous Gyr-long phase of mass accretion from an evolved companion. According to the recycling scenario (Alpar et al. 1982; Backer et al. 1982) during the accretion phase, MSP binaries were low-mass X-ray binaries (LMXBs) and turned into radio and gamma-ray pulsars when mass accretion ceased. The first evidence of a transition between the two states was discovered in the radio MSP binary PSR J1023+0038 that was found in an accretion disc state between 2001 and 2004 (Archibald et al. 2009) and entered again in an LMXB state in 2013 (Patruno et al. 2014; Stappers et al. 2014; Bogdanov et al. 2015). Similar transitions were also observed in IGR J1825–2452, in the M28 globular cluster (Papitto et al. 2013) and in the Galactic field X-ray source XSS J12270–4859 (henceforth J1227) (Bassa et al. 2014; Bogdanov et al.

★ E-mail: demartino@oacn.inaf.it

2014; de Martino et al. 2014). The transitions occurred on time-scales much shorter than secular evolution, likely controlled by variations in the mass transfer rate from the late-type companion. These three systems, dubbed transitional MSPs (tMSPs), harbour non-degenerate companions in tight (5–12 h) orbits and fall in the increasing class of redbacks (RB) (14 confirmed so far with $M_2 \sim 0.2$–$0.4\,M_\odot$) as opposed to those dubbed black widows (BW) containing degenerate companions with $M_2 \ll 0.1\,M_\odot$ (Roberts et al. 2015; Strader et al. 2019).

Transitional systems are enigmatic and complex binaries. During the LMXB state they display peculiar behaviour from radio, optical up to X-ray and gamma-rays (de Martino et al. 2010, 2013; Archibald et al. 2015; Papitto et al. 2015; Ambrosino et al. 2017; Bogdanov et al. 2018; Papitto et al. 2019). Only IGR J1825–2452 displayed an outburst (Papitto et al. 2013), while the other two were never recorded in such state. When in the disc state, tMSPs are characterized by a subluminous X-ray emission ($L_X \sim 10^{33}$–10^{34} erg s^{-1}) with high, low, and flare 'modes' (Linares 2014). In IGR J1825–2452 and PSR J1023+0038, the X-ray low modes were found to be accompanied by radio flares in quasi-simultaneous observations (Ferrigno et al. 2014; Bogdanov et al. 2018), possibly due to outflowing material. Additionally, the presence of X-ray pulses during high X-ray modes in PSRJ1023+0038 (Archibald et al. 2015) and J1227 (Papitto et al. 2015) was interpreted as signature of accretion on to the NS. This interpretation is challenged by the detection of optical pulsations (Ambrosino et al. 2017) that cannot be ascribed to accretion. The optical and X-ray pulsations were recently detected simultaneously during the high X-ray modes (Papitto et al. 2019). Instead, during flares lower amplitude optical pulses were also detected but not in the X-rays.

A variety of interpretation have been proposed for the complex behaviour during the LMXB state: an enshrouded pulsar (Coti Zelati et al. 2014; Takata et al. 2014), a pulsar in a propeller state (Papitto et al. 2014; Papitto & Torres 2015), an intermittent propellering radio pulsar (Ertan 2017) or a low accretion rate pulsar from a trapped disc near corotation (D'Angelo & Spruit 2012) (see also Campana & Di Salvo 2018, for a review). Whether the disc shocks with a striped pulsar wind at a few light cylinder radii away from the pulsar, giving rise synchrotron emission producing the optical and X-ray pulses, is a challenging interpretation put forward by Papitto et al. (2019) (see also Campana et al. 2019; Veledina, Nättilä & Beloborodov 2019).

In the rotation-powered (RMSP) state transitional systems behave as all other RB binaries (Roberts et al. 2015, 2018), displaying long radio eclipses, up to 60 per cent of the orbit, due to the passage of the NS through ionized material surrounding the companion, likely in the form of an intrabinary shock (IBS) produced by the interaction of the pulsar wind with that of the late-type star. The shock is also expected to emit a non-thermal spectrum and to produce a large X-ray orbital modulation (Arons & Tavani 1993). Such modulations are indeed observed in both RBs and BWs, with the difference that the X-ray orbital maximum occurs at the inferior conjunction of the NS in the former group and vice versa in the latter. To explain the opposite phasing of the X-ray maxima and since RBs are expected to possess stronger winds than the BWs, the shock would be oriented towards the pulsar in the RBs but towards the companion star in BWs (Roberts et al. 2015; Romani & Sanchez 2016; Wadiasingh et al. 2017).

When in RMSP state, X-ray msec pulses were observed in PSRJ1023+0038 at a few per cent ($\sim$ 10 per cent, rms) level (Archibald et al. 2010) and remain still undetected in J1227 (Papitto et al. 2015). Instead gamma-ray pulsations were detected with *Fermi*-LAT in J1227 at 5σ level nearly in phase with the high-frequency (1.4 GHz) radio pulses, indicating an origin in the pulsar magnetosphere (Venter, Johnson & Harding 2012; Johnson et al. 2014, 2015). In PSR J1023+0038 only a weak evidence of gamma-ray pulses was found at 3.7σ level (Archibald et al. 2013). We also note here that the gamma-ray and X-ray fluxes changed by a few 3–10 times between the LMXB and RMSP states in J1227 and PSRJ1023+0038, respectively (Torres et al. 2017).

How transitions occur and whether all RBs could be tMSPs is a key issue to be investigated yet. The study of the long-term behaviour, especially in the X-ray band where the IBS is expected to dominate, may be a powerful means to infer changes in the shock geometry and in turn the mass accretion rate. Also, the level of irradiation of the donor star is a key ingredient in understanding whether RBs could be prone to perform transitions. In fact, orbital modulations in the optical range (e.g. Thorstensen & Armstrong 2005; de Martino et al. 2015; Hui et al. 2015; Romani et al. 2015; Bellm et al. 2016; Al Noori et al. 2018) reveal in some systems, such as PSR J1023+0038, J1227, PSR J2215+51, and PSR J2339–0533, strong heating of the companion, while others, despite displaying significant X-ray orbital modulations, such as PSR J2129–0429, have companions suffering little irradiation.

Of the two known tMSPs in the field, PSR J1023+0038 is currently in an LMXB state (see Papitto et al. 2019, for latest results), while J1227 is in a radio-pulsar state (Bassa et al. 2014; Roy et al. 2015). Both systems have NS spinning at similar periods (1.69 ms). After the transition to the RMSP state occurred in late 2012 to early 2013, the soft (0.3–10 keV) X-ray emission of J1227 was studied by Bogdanov et al. (2014) and de Martino et al. (2015). The spectrum was found to be non-thermal with a power-law photon index $\Gamma \sim 1.1$, harder than that ($\sim$1.7) observed during the LMXB state (de Martino et al. 2010, 2013). The X-ray emission was variable at the 6.91 h orbital period. Comparison of the two observations performed in 2013 December and 2014 June, showed that the amplitude of the orbital modulation changed by a factor of $\sim$2 (de Martino et al. 2015). This variability was surprisingly anticorrelated with the simultaneous optical *U*-band light curve, where instead the modulation decreased by a factor of 2. This suggested a variability in the IBS over a time-scale of a few months. The hard spectral shape in the soft range is similar to other RBs, with a few also observed above 10 keV and detected up to 40–70 keV without displaying a spectral break (Tendulkar et al. 2014; Kong et al. 2017; Al Noori et al. 2018; Kandel, Romani & An 2019).

We here present the first hard X-ray study of J1227 during its current rotation-powered state based on an observation performed with the *NuSTAR* satellite. We complement the analysis using previous *XMM–Newton* and archival Neil Gehrels *Swift* (henceforth *Swift*) data for a comparison among different epochs. We also report on the radio monitoring programme conducted at the *Parkes* telescope over 2.5 yr that also gives a contemporaneous coverage with the *NuSTAR* observation. In Section 2, we report the radio observations and analysis. In Section 3, the X-ray observation are described and the timing and spectroscopic analyses are reported in Sections 4 and 5, respectively. The results are discussed in Section 6.

2 THE RADIO MONITORING

J1227 was observed monthly at the *Parkes* 64 m radio telescope from 2014 June to 2017 February, as part of the project P880. Data were acquired mainly around 1.4 GHz with the central beam

Table 1. Main parameters of the observing systems adopted at the Parkes telescope. The backend name is listed in column 1, while columns 2–5 report the central frequency, the bandwidth and the number of frequency channels used. For search mode observations, column 5 reports the sampling time in μs, while, for folding mode ones, the number of profile bins.

Backend	ν_c (MHz)	Bandwith (MHz)	N_{chan}	t_{samp}/N_{bin}
BPSR	1352	340	870	64 μs
DFB4	1369	256	1024	100 μs
	1369	256	512/1024	256/512
	3100	1024	512	128 μs
	3100	1024	1024	256
CASPSR	1352	340	435	128
	728	64	82	128

of the 20 cm multibeam receiver (Staveley-Smith et al. 1996) or, when unavailable, with the H-OH receiver.[1] A small number of data were obtained simultaneously around 3.1 GHz (10 cm) and 0.7 GHz (50 cm) using the coaxial 1050 cm receiver. Most observations were carried out in search mode (with folding of the data being done off-line to correct for possible orbital period variations) using either the BPSR digital signal processor (Keith et al. 2010) or the DFB4[2] and, in parallel, CASPSR, the CASPER *Parkes* Swinburne Recorder[3] in folding mode and applying coherently dedispersion. Table 1 summarizes the main parameters.

The observations were planned in such a way as to avoid those orbital phases in which the pulsar was likely to be completely eclipsed, but also to start or finish close eclipse ingress or egress, to monitor the possible variability of the eclipse extent. The orbital phases were predicted on the basis of orbital ephemeris constantly updated during the observing project. Fig. 1 shows the observations (dashed lines) and detections (solid lines) at the three observed frequencies. The test pulsar was clearly detected, excluding a malfunctioning of the acquisition system. The eclipse extends at least between phases 0.07 and 0.39, but shows a large variability in time, with the pulsar being sometimes undetectable for the entire orbit. The pulsar was seen only seldom at frequencies different from 1.4 GHz: at 0.7 GHz, radio frequency interferences and absorption of the signal from the surrounding medium likely play a major role in the non-detections; at 3.1 GHz it is barely detectable possibly due to the intrinsic spectrum of the source. A measurement of the spectral index of J1227 with our data set is, however, not possible since most of the data are uncalibrated and because the source is highly variable also far from eclipses, with a signal-to-noise ratio varying by a factor up to 5 at 1.4 GHz. Because of this, the measurement of the flux density is very uncertain, preventing us to give meaningful constraints on the spectral index. We also here recall that previous observations at frequencies above 1.4 GHz only provided upper limits to the flux (Bassa et al. 2014).

2.1 The radio ephemeris

Timing analysis was carried out on the 20 cm data using only the data with orbital phases outside the range between 0.05 and 0.4, in order to exclude points affected by extra dispersive delays due to the eclipsing material. A profile template was created by adding in phase several observations together (for a total of about 40 h). One or more times of arrival (ToAs) were then created by cross-correlation of the standard profile with each observing epoch. Usually a ToA was computed for every 15 min of observation, but in some cases, depending on the intensity of the signal, we used data segments from 5 to 60 min in length. The above steps were carried out using the software PSRCHIVE.[4] The timing analysis was done with TEMPO2 (Hobbs, Edwards & Manchester 2006). Table 2 reports the radio

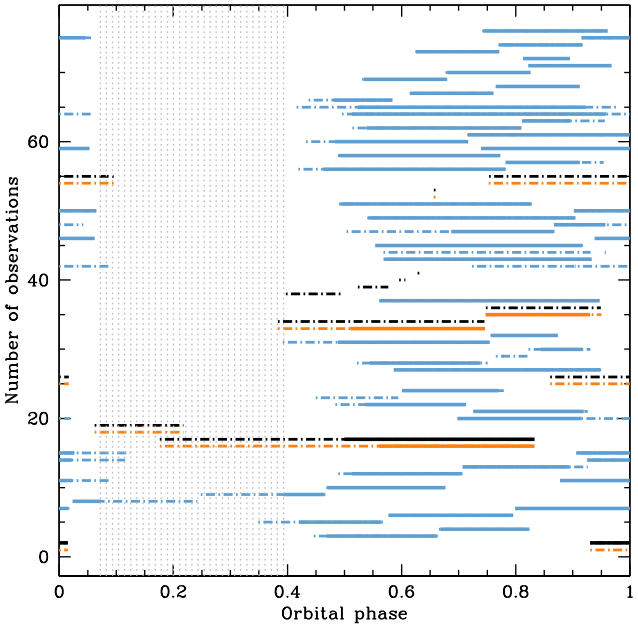

Figure 1. Summary of all the observation (dashed lines) and detections (solid lines) performed at *Parkes* as part of P880. The observations at 20 cm (1.4 GHz) are plotted in light blue, those at 10 cm (3.1 GHz) in black, and those at 50 cm (0.7 GHz) in orange. The grey dotted area marks the orbital phases where the pulsar was never detected.

Table 2. Timing parameters of PSR J1227–4853 obtained from the 20 cm *Parkes* data over the entire 2.5 yr dataspan. Timing results are in barycentric dynamical time.

Parameter	Value[a]
RA (J2000) (h:m:s)	12:27:58.7186(4)
Dec. (J2000) (d:m:s)	−48:53:42.707(5)
Pulsar frequency f (Hz)	592.98777342489(14)
Frequency derivative $\dot{f}$ (Hz s^{-1})	$-4.619(11) \times 10^{-15}$
Period epoch (MJD)	57180
Dispersion measure (pc cm^{-3})	43.423(3)
Binary model	BTX
Orbital period P_b (d)	0.287887802(5)
Orbital frequency f_b (Hz)	$4.02034315(11) \times 10^{-5}$
Orbital frequency derivative $\dot{f}_b$ (s^{-2})	$3.74(6) \times 10^{-18}$
Orbital frequency second derivative $\ddot{f}_b$ (s^{-3})	$-7.77(11) \times 10^{-26}$
Epoch of NS ascending node T_{asc} (MJD)	56700.907021(4)
Projected semimajor axis $a1$ (lt-s)	0.668492(14)
Span of timing data (MJD)	56824.257–57685.210
Number of TOAs	593
Post-fit residuals rms (μs)	49.858

[a] 2σ errors on the last quoted digit(s).

[1] https://www.parkes.atnf.csiro.au/observing/documentation/
[2] http://www.jb.man.ac.uk/pulsar/observing/DFB.pdf
[3] http://astronomy.swin.edu.au/pulsar/?topic = caspsr
[4] http://psrchive.sourceforge.net/

Table 3. Timing ephemeris obtained from the 20 cm *Parkes* data over ∼170 d around the *NuSTAR* observation. The parameters reported are as in Table 2.

Parameter	Value
RA (J2000) (h:m:s)	12:27:58.7194(14)
Dec. (J2000) (d:m:s)	−48:53:42.712(19)
Pulsar frequency f (Hz)	592.9877734395(9)
Frequency derivative $\dot{f}$ (Hz s^{-1})	$-4.3(3) \times 10^{-15}$
Period epoch (MJD)	57139
Dispersion measure (pc cm^{-3})	43.423(3)
Binary model	BT
Orbital period P_b (d)	0.287887065(5)
Orbital period derivative $\dot{P}_b$	$-2.5(14) \times 10^{-10}$
Epoch of NS ascending node T_{asc} (MJD)	57139.0715595(6)
Projected semimajor axis $a1$ (lt-s)	0.668482(16)
Span of timing data (MJD)	57063.530–57233.225
Number of TOAs	189
Post-fit residuals rms (μs)	23.097

ephemeris obtained with the from the full 20 cm *Parkes* data set spanning 2.5 yr. The inclusion of two orbital frequency derivatives was necessary to flatten the timing residuals and thus we adopted the *BTX* binary model.[5] The planetary ephemeris DE405 (Standish 1998) and the TT(TAI) time standard (e.g. Lorimer & Kramer 2005) were used. This ephemeris is in accord within errors with those reported by Roy et al. (2015), who instead adopted the *ELL*1 binary model over a timespan of 270 d. The *BT* model, including just the first derivative of the orbital period, was used on dataspans up to 300 d. After that, orbital trends clearly affected the timing residuals. The *BT* model, however, resulted in an rms comparable to that reported in Table 2, for dataspans as long as 600 d, after which higher order derivatives were needed to phase connect further data points.

In order to properly fold the X-ray data presented here, we also created a more local timing solution using approximately 170 d of *Parkes* data around the *NuSTAR* observation. Only one orbital period derivative was needed to properly phase connect the data on this shorter timespan and therefore we used binary model BT. The related ephemeris are shown in Table 3.

2.2 Distance estimates

The dispersion measure (DM) has been evaluated using a few measures at 50 cm avoiding eclipses resulting in DM = 43.423(3) pc cm^{-3}, where here uncertainty is at 2σ level. It has then been kept fixed in the analysis of the other data sets at 20 cm. This determination, although at lower accuracy, is in agreement with that previously derived (43.4235(7)) (Roy et al. 2015). The DM value, when adopting Cordes & Lazio (2002) model of the Galactic electron density distribution, gives a distance of 1.4 kpc (Roy et al. 2015). However as noted by Jennings et al. (2018), the DM-based distances calculated using either Cordes & Lazio (2002) or Yao, Manchester & Wang (2017) models are on average slightly underestimated. For J1227 there is no parallax measurement from radio observations yet. However, the recent release of *Gaia* DR2 parallaxes (Gaia Collaboration 2018) allows to obtain first direct distance measures for MSP binaries with relatively bright optical companions. J1227 has a parallax measure $\tilde{\pi} = 0.624 \pm 0.168$ mas that, accounting for the DR2 parallax average zero-point offset of −0.029 mas (see Lindegren et al. 2018), translates into a distance $d_{\tilde{\pi}} = 1.53 \pm 0.39$ kpc. However, reliable distance estimates should account for the space density distribution of the objects. Adopting a weak distance prior that varies as a function of Galactic longitude and latitude according to the Galactic model described in (Bailer-Jones et al. 2018),[6] we estimate a distance of $D_{BJ} = 1.51^{+0.59}_{-0.35}$ kpc, taking into account the average zero-point offset. On the other hand adopting a distance prior based on the Galactic pulsar population of Lorimer et al. (2006) and also accounting for the average zero-point offset, Jennings et al. (2018) derive $D_L = 1.37^{+0.69}_{-0.15}$ kpc. The two estimates agree within their 1σ uncertainties. We then adopt the latter distance for J1227.

We also estimate the intrinsic spin-down power, $\dot{E} = 4\pi^2 I \dot{P}/P^3$, where P and $\dot{P}$ are the spin period and its derivative and $I \simeq (M_{NS}/1.4\,M_\odot)(R_{NS}/10\,\mathrm{km})\,10^{45}$ g cm^{-2} is the momentum of inertia of the NS. We use the refined pulsar spin frequency and first derivative (Table 2) that are more accurate than those derived by Roy et al. (2015), which were based on a shorter, 270 d, timespan. With the accurate *Gaia* DR2 proper motion ($\mu = 20.13(23)$ mas yr^{-1}), we correct the observed $\dot{P}$ for the Shklovskii effect: $\dot{P}_{Sh}/P = v_t^2/c\,D$, where v_t is the transverse velocity. For a distance of 1.37 kpc, we derive $\dot{P}_{corr} = \dot{P}_{obs} - \dot{P}_{Sh} = 1.086(2) \times 10^{-20}$. Correspondingly, adopting a NS with 1.4 $M_\odot$ and 10 km radius, we derive $\dot{E} = 8.94(2) \times 10^{34}$ erg s^{-1}. As a comparison, Roy et al. (2015) derived $\dot{E} = 9.0(8) \times 10^{34}$ erg s^{-1}. However, allowing the full range of uncertainties in the distance D_L, we obtain $\dot{E} = 8.9^{+0.2}_{-0.9} \times 10^{34}$ erg s^{-1}.

3 THE *NuSTAR* OBSERVATION

J1227 was observed by *NuSTAR* (Harrison et al. 2013) from 2015 April 26 to 28 with both telescope modules FPMA and FPMB, covering 171.8 ks, for a total effective exposure time of 96.4 ks (OBSID: 30101033002).

The processing and filtering of the *NuSTAR* photon event data was performed with the standard *NuSTAR* pipeline (NUSTARDAS) version v1.8.0 with calibration data CALDB 20190503. The source photon events were extracted from circular regions of 25 pixels (61 arcsec) radius and the background from a region of 50 pixels in a source-free region. Photon event arrival times from both FPMA and FPMB were corrected to the Solar system barycentre using the JPL DE405 ephemeris using the radio position reported in Table 2. Combined net light curves were constructed by subtracting the source light curves for the corresponding background in each FPMA and FPMB module and averaged together. The source was detected at an average net count rate of 0.037±0.004 cts s^{-1} in the 3–79 keV range. Spectra from the two telescope modules were extracted using the NUPRODUCTS and then binned to achieve a minimum of 35 photons per bin. All photons below 3 keV (channel 35) and above 79 keV (channel 1935) were flagged as bad.

4 TIMING ANALYSIS

4.1 The X-ray variability

The combined (FPMA and FPMB) net X-ray light curve in the 3–79 keV range (Fig. 2) shows variations in the count rate over the 47 h-long observation on time-scale of ∼7 h, consistent with the 6.91 h orbital period. Neither flaring activity nor sudden drops in the

[5] Binary models are described at http://tempo.sourceforge.net/ref_man_sections/binary.txt

[6] http://gaia.ari.uni-heidelberg.de/tap.html

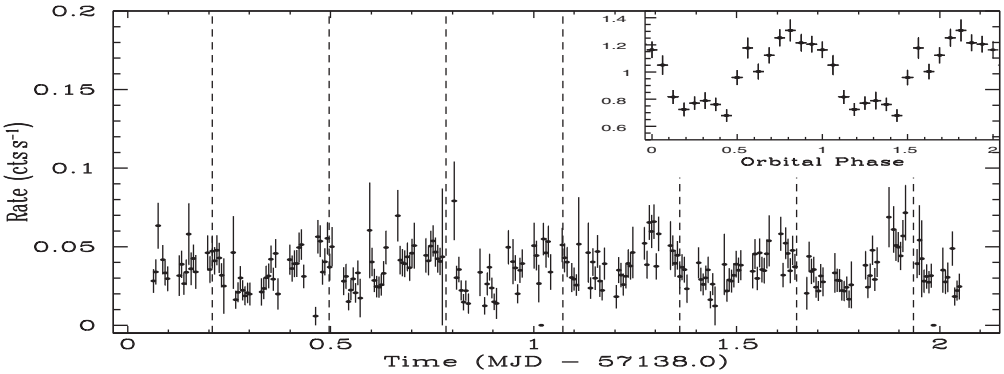

Figure 2. The background subtracted *NuSTAR* light curve of J1227 binned at 500 s in the 3–79 keV energy range. The periodic gaps in the data are due to the Earth occultation of the source. The vertical dashed lines show the times of the passage of the pulsar at the ascending node of the orbit (T_{asc}) adopting the orbital radio ephemeris reported in Table 3. The inset shows the 3–79 keV normalized light curve folded at the 6.91 h orbital period binned in 16 phase intervals. Phase zero corresponds to the passage of the NS at the ascending node of the orbit.

count rate are observed throughout the observation. A search for orbital modulation was carried out by performing Fourier analysis on the barycentred corrected light curve in the 3–79 keV range adopting a time bin of 340 s. A strong peak at ∼25 000 s as well as minor peaks at the beat frequency of the *NuSTAR* spacecraft are detected. A sinusoidal fit to the light curve gives a period of 25060 ± 235s (1σ confidence level) ($\chi^2_\nu = 1.08$, d.o.f. = 319). An epoch-folding method (Leahy 1987) was also applied, adopting eight orbital phase bins using various trial periods around the radio nominal period of 24 873 s with a period resolution of 50s. The χ^2 distribution shows a peak at 9σ level at a period of 25 232 ± 90 s as evaluated from a Gaussian fit. These determinations of the period are however consistent within their 1σ and 3σ uncertainties with the accurate radio orbital period reported in Tables 2 and 3, respectively. No cycle to cycle variation is observed in the average count rate level over the ∼6.9 orbital cycles covered by the *NuSTAR* observation (see Fig. 2).

The FPMA and FPMB background subtracted light curves in different energy ranges were then merged and folded at the binary orbital period $P_b = 24873.4424$ s, adopting as phase $\Phi_{orb} = 0.0$ the time of passage of the pulsar at the ascending node $T_{asc} = 57139.0715595$ (MJD), reported in Table 3. The folded light curve in the 3–79 keV band, evaluated over 16 phase bins (see inset in Fig. 2), shows a structured broad maximum at orbital phase ∼0.8 and a minimum at ∼0.25, close to the inferior and superior conjunction of the pulsar, respectively. The fractional amplitude, defined as $(F_{max} - F_{min})/(F_{max} + F_{min})$, where F_{max} and F_{min} are the maximum and minimum count rates detected in the light curve, respectively, is 28(3) per cent. The rise to the maximum is slower than the subsequent decay, reaching a peak at $\Phi_{orb} = 0.9$. Also the minimum is not smooth or flat-bottom but rather structured towards the rise to the maximum. A well-defined double-peaked maximum, as observed in 2014 June by *XMM–Newton* (de Martino et al. 2015), is not present. The modulation also appears different from those observed in 2013 December and 2014 January by *XMM–Newton* and *Chandra*, respectively, which instead are similar to each other (see Bogdanov et al. 2014; de Martino et al. 2015).[7]

A close comparison of the *NuSTAR* data with the two *XMM–Newton* EPIC-MOS[8] observations is made by folding background subtracted light curves in a common 3–12 keV energy range using T_{asc} and P_b reported in Table 2. These are shown in Fig. 3. The orbital modulation is clearly structured in all data sets but shows differences especially in the broad maximum. The fractional amplitude of the orbital modulation increases from 34(8) per cent in 2013 December to 67(9) per cent in 2014 June and decreases again to 36(2) per cent in 2015 April. Here, we note that the flux at minimum is about the same at all epochs, $F_x \sim (2.0–2.5) \times 10^{-13}$ erg cm^{-2} s^{-1}. While the variability in amplitudes between the first two observations was already reported in de Martino et al. (2015), the *NuSTAR* observation confirms that modulation amplitudes have not stabilized after the transition from a disc to a rotation-powered state, hinting to a non-stationary IBS emission. Noteworthy is the change in the shape of the maximum among the three epochs, displaying a local peak at Φ_{orb} ∼0.7 in 2013, a double-peaked maximum in 2014 centred at Φ_{orb} ∼0.75 and a local peak at Φ_{orb} ∼0.9 in 2015. Since a simple sinusoid at the orbital frequency does not satisfactory fit the light curves in the 3–12keV range, a fit was performed using a composite function consisting of two or three sinusoids at the fundamental frequency, f_b, and its two higher harmonics, $2f_b$ and $3f_b$ (see Table 4). Only for the 2014 data set three components are required, while for the other two epochs two sinusoids at f_b and $2f_b$ well describe

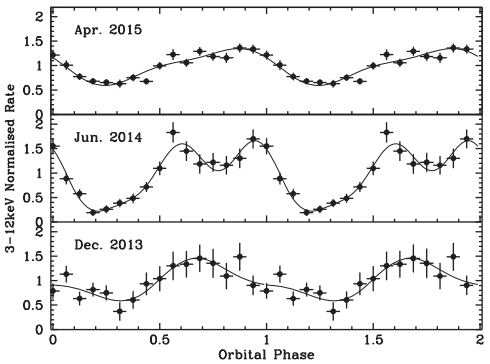

Figure 3. Comparison of the background subtracted orbital folded light curves, evaluated over 16 phase bins, as observed by *XMM–Newton* in 2013 December and 2014 June and by *NuSTAR* in 2015 April, in the common energy range 3–12 keV. The light curves are normalized for a direct comparison. Composite sinusoidal fits using two (2013 December and 2015 April) or three (2014 June) frequencies, the fundamental f_b and two harmonics $2f_b$ and $3f_b$, are also shown for each data set.

[7]The short *Chandra* observation is not used here.

[8]Details of the reduction and extraction of the EPIC-MOS1,2 (Turner et al. 2001) cameras are published in de Martino et al. (2015).

Table 4. Summary of sinusoidal fits to the X-ray folded orbital light curves in selected energy bands.

Year	Band (keV)	Flux[a]	Multisinusoidal fit							Single sinusoidal fit		
			A_{f_b}	Φ_{f_b}	A_{2f_b}	Φ_{2f_b}	A_{3f_b}	Φ_{3f_b}	χ^2_ν/d.o.f.	A_{f_b}	Φ_{f_b}	χ^2_ν/d.o.f.
2013	3–12	3.8(4)	0.37(7)	0.52(3)	0.13(6)	0.48(4)	–	–	0.89/11	0.34(8)	0.51(9)	1.30/13
	0.3–3	1.4(1)	0.22(5)	0.50(1)	0.11(5)	0.38(7)	–	–	1.00/11	0.25(5)	0.49(1)	1.53/13
	3–6	1.3(1)	0.36(8)	0.53(3)	0.10(7)	0.47(7)	–	–	1.01/11	0.35(7)	0.52(2)	1.03/13
	6–12	2.4(3)	–	–	–	–	–	–	–	0.4(2)	0.48(6)	2.5/13
2014	3–12	6.0(4)	0.57(5)	0.48(1)	0.33(5)	0.36(2)	0.19(4)	0.23(3)	0.80/11	0.67(9)	0.49(1)	3.92/13
	0.3–3	1.9(1)	0.47(3)	0.49(2)	0.27(3)	0.39(4)	0.19(3)	0.21(3)	0.79/11	0.54(8)	0.49(1)	5.53/13
	3–6	2.1(1)	0.60(5)	0.49(3)	0.33(5)	0.36(9)	0.19(4)	0.24(4)	0.63/11	0.71(9)	0.50(2)	3.11/13
	6–12	3.9(4)	0.46(11)	0.45(4)	0.33(11)	0.37(6)	0.27(10)	0.22(6)	0.86/11	0.52(14)	0.47(2)	1.41/13
2015	3–12	4.7(3)	0.34(4)	0.46(2)	0.10(3)	0.35(1)	–	–	0.38/11	0.36(2)	0.49(1)	0.60/13
	3–6	1.7(2)	0.28(5)	0.45(3)	0.14(5)	0.32(6)	–	–	1.33/11	0.29(4)	0.46(2)	1.87/13
	6–12	3.1(2)	–	–	–	–	–	–	–	0.39(3)	0.47(1)	1.42/13
	12–25	5.8(2)	0.36(2)	0.44(1)	0.14(2)	0.36(1)	–	–	0.54/11	0.34(3)	0.44(1)	1.05/13
	25–79	19.8(1)	–	–	–	–	–	–	–	–	–	–

[a] Average unabsorbed fluxes in units of 10^{-13} erg cm^{-2} s^{-1} in selected energy bands as derived from spectral fits to the average spectra at each epoch.

the orbital modulation, although the improvement over a single sinusoid is significant only at $\sim$ 90 per cent and 92 per cent level for the 2013 and 2015 epochs, respectively. The amplitudes of the sine components at f_b and $2f_b$ are similar in 2013 and 2015 within their uncertainties. An offset by 0.13 in phase is derived in the $2f_b$ component between these two epochs but not in the fundamental that remains stable within errors. Different is the case observed in 2014 where f_b and $2f_b$ increase in amplitude by a factor of 1.7 and of 3, respectively. The $3f_b$ component has a fractional amplitude of $\sim$ 20 per cent and contributes at the minimum of the modulation.

A further comparison is carried out using common selected energy ranges between the *XMM–Newton* and *NuSTAR* data, namely 3–6 and 6–12 keV for the three epochs. Folded light curves in the soft 0.3–3 keV bands were also produced for the two *XMM–Newton* data sets to inspect the energy dependence of the orbital variability. Table 4 reports the results of the fits by using up to three components. In Fig. 4, the energy resolved light curves in the three energy ranges are shown for the two earlier epochs. Two sine components better describe the orbital modulation in the softer 0.3–3 and 3–6 keV bands in 2013 December, although the improvement over a single sinusoid is significant only at $\sim$ 96 per cent and at $\sim$ 64 per cent, respectively. At higher (6–12 keV) energies the variability is badly defined in 2013, though consistent with that observed by *NuSTAR* in 2015.

As for 2014 June, three sinusoids are required in all bands. As before, the amplitudes of the fundamental f_b frequency change by a factor of about 2 while that of $2f_b$ increases by $\sim$3 in all bands with respect to the 2013 and 2015 observations. The modulation is stronger in the 3–6 keV range, while in the 6–12 keV band, it is badly defined and consistent with the softer ranges within uncertainties. This produces a mild hardening between 0.3–3 and 3–6 keV ranges at $\Phi_{orb} \sim 0.75$, i.e. at the inferior conjunction of the NS. This behaviour is seen in the hardness ratios (HR), defined as the ratio of count rates in the 3–6 and 0.3–3 keV bands and 6–12 and 3–6 keV ranges. At higher energies the HR are instead dominated by noise (see Fig. 5). The significance of the orbital variability of the HR, defined as the ratio of count rates in the 3–6 and 0.3–3 keV bands and 6–12 and 3–6 keV ranges, was inspected by modelling the orbital HR curves with a constant and a sinusoidal function. For the 2014 June observation, and for the softer HR between 3–6 and 0.3–3 keV we obtained $\chi^2 = 10.7$, d.o.f. = 15 in case of a constant and $\chi^2 = 6.5$, d.o.f. = 13 for a sinusoidal fit with fractional amplitude of 17(6) per cent. The improvement of the modelling with respect to a constant was however at only 2σ level. For the 2013 December observations and for the same soft HR we obtained in the case of a constant $\chi^2 = 12.95$, d.o.f. = 15 and $\chi^2 = 6.3$, d.o.f. = 13 for a fit with a sinusoid with fractional amplitude of 15(5) per cent. The variability is significant at only 2.6σ level. The HR at higher energies between 3–6 and 6–12 keV are instead consistent with a constant in both 2013 and 2014 observations (see Fig. 5). This refines the results found by de Martino et al. (2015), where hardness ratios were inspected in 0.3–2 and 2–10 keV.

The *NuSTAR* orbital light curves of 2015 April were also produced in the 12–25, 25–40, 40–79, and 25–79 keV ranges (see Fig. 6). A weaker modulation than that observed in 2014 June, but of similar amplitude as in 2013 December ($\sim$ 30 per cent), is detected below 12 keV. The modulation extends up to $\sim$25 keV with similar fractional amplitudes. It is however undetected at higher energies with an upper limit to the modulation amplitude of $\sim$ 10 per cent (3σ confidence level). Two harmonics account for the asymmetric shape in the 3–6 and 12–25 keV range although significant at 92 per cent and 97 per cent confidence levels, respectively. In the 6–12 keV range only the fundamental frequency is required (see Table 4). The hardness ratios in the four selected bands reveal no spectral variations except at higher energies due to the lack of detectable modulation above 25 keV (right-hand panel in Fig. 6).

We also performed a Fourier search for coherent periodicities in the 3–79 keV time-series recorded by both *NuSTAR* modules, after preliminarily correcting the photons times of arrival for the orbital motion of the pulsar using the orbital parameters listed in Table 3. The *NuSTAR* onboard clock suffers of timing jumps introducing spurious derivatives of the order of 10^{-10} Hz s^{-1} of the frequency of a $\sim$600 Hz coherent signal (see Sanna et al. 2017). Therefore, a search was done over a frequency range of $\pm 10^{-4}$ Hz around the spin frequency of J1227. The maximum value of the Fourier power density observed corresponds to an upper limit on the rms pulse amplitude of 8.8 per cent (3σ confidence level; see Vaughan et al. 1994). This value is comparable with the upper limit set from the analysis of *XMM–Newton* observation performed in 2014 (7.1 per cent; Papitto et al. 2015) and slightly smaller than the amplitude of 11 ± 2 per cent of the pulses detected in the 0.25–2.5 keV band during the radio pulsar state of PSR J1023+0038 (Archibald et al. 2010).

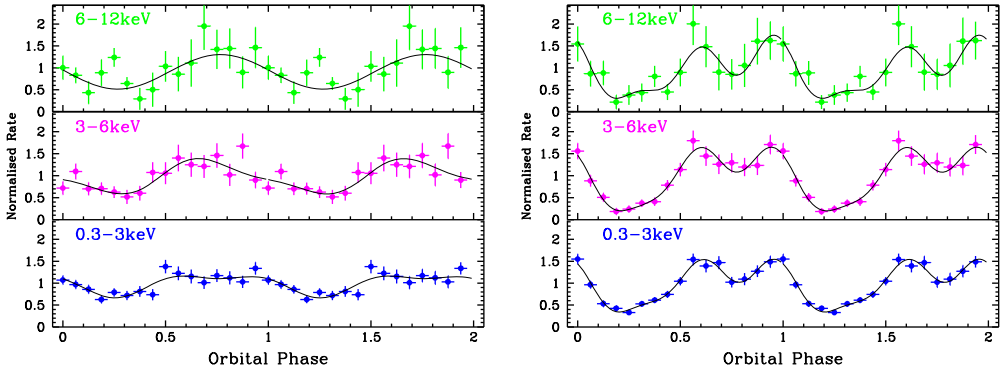

Figure 4. Energy resolved light curves folded at the 6.91 h orbital period in selected bands evaluated over 16 phase bins, as observed with *XMM–Newton* in 2013 December (*left-hand panel*) and in 2014 June (*right-hand panel*). For the former epoch, a composite sinusoidal fit with two components is also shown for the softer bands while only the fundamental is shown for the harder 6–12 keV range. Instead, three sinusoids are required for the second observation. Ordinates are normalized to unity.

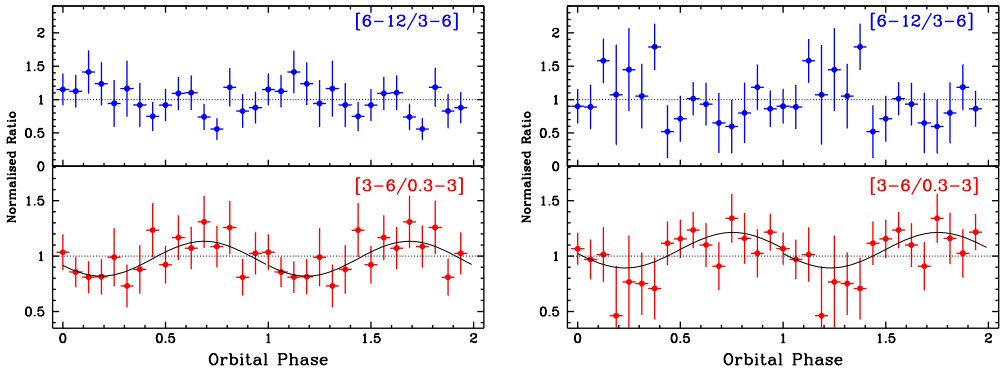

Figure 5. Hardness ratios folded at the 6.91 h orbital period in the 0.3–3, 3–6, and 6–12 keV ranges evaluated over 16 phase bins as observed by *XMM–Newton* in 2013 December (*left*) and in 2014 June (*right*). A sinusoidal function (black) is also shown to help visualization for the mild hardening between the soft 0.3–3 keV and medium 3–6 keV ranges (bottom panels) although significance of the variability is below 3σ (see the text for details). Ordinates are normalized to unity.

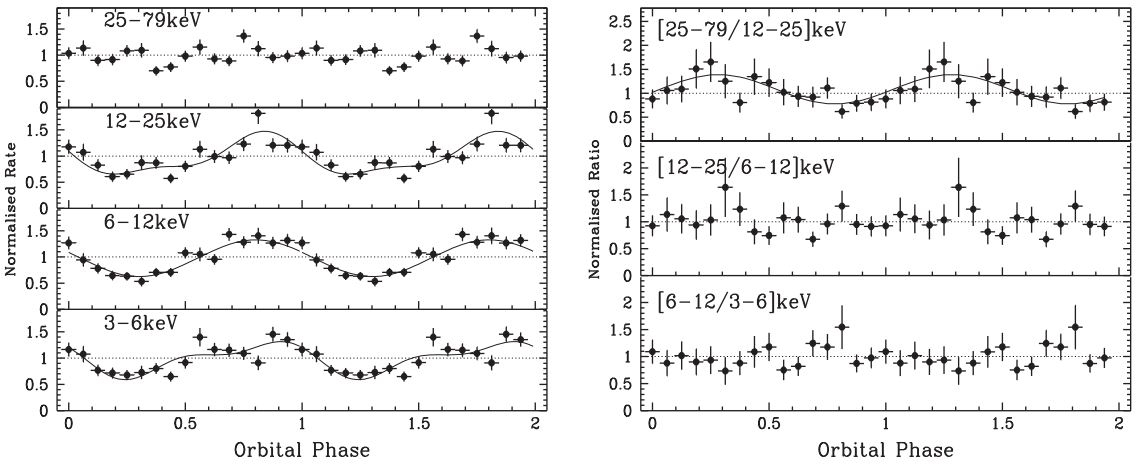

Figure 6. *Left:* Folded orbital light curves in selected energy bands and evaluated in 16 phase bins as observed by *NuSTAR* in 2015 April. A composite sinusoidal fit with one or two harmonics (see Table 4) is also shown, except for the harder band 25–79 keV where no modulation is detected. *Right:* Hardness ratios remain constant except in the hardest range due to the lack of detection of orbital variability. Ordinates are normalized to unity.

4.2 The optical variability

The optical long-term behaviour of J1227 was also inspected by extending the comparison of the orbital modulations between the X-ray and optical ranges at the epoch of the *NuSTAR* observation. In particular, the optical *U*-band modulation decreased by a factor of ∼2 between the *XMM–Newton* pointings in 2013 December and 2014 June and accompanied by an anticorrelation in the X-ray band (de Martino et al. 2015). Therefore, *U*-band photometry

was extracted using *Swift* UVOT (Roming et al. 2005) observations acquired between 2015 January and November. This larger timespan was dictated by the occasional coverage with the *U* filter. As an additional comparison *U*-band measures were also extracted for several epochs, namely 2013 December–2014 January, 2014 March–August, and 2014 September–November to trace potential changes in the optical light curve over different epochs. For this purpose, we used the tool UVOTMAGHIST in FTOOLS v.6.22, accounting for sensitivity UVOT patches,[9] to extract the photometry and applied the correction to the Solar system barycentre. The folded light curves were then compared with those observed in 2013 and 2014 by the optical monitor (OM) onboard *XMM–Newton*. The modulation observed during the 2015 January–November has a peak-to-peak amplitude of 1.47(8) mag, similar to that observed in 2013 December by the OM (1.43(4) mag) and to those observed by UVOT in the same period (2013 December–2014 January) and in 2014 September–November. It is thus larger by a factor of ∼2 than that observed in 2014 Junuary by the OM (0.72(9) mag) and by UVOT in the 2014 March–August (see Fig. 7). This indicates that the smaller orbital *U*-band modulation amplitude was only reached during the 2014 March–August period, whilst before and after that epoch the variability was larger. Here, we also confirm that J1227 shows within uncertainties of the photometry the same minimum optical flux at all epochs ($U \sim 20.5$). The decrease and the subsequent increase in amplitude in 2014 thus occurred over a time-scale of ∼2 and 1 month, respectively. Comparing the optical and X-ray behaviour in the 2013, 2014, and 2015 epochs, we can firmly confirm the orbital modulation is anticorrelated in the two energy regimes, i.e. when the X-ray modulation is larger, the optical *U*-band orbital variability is smaller.

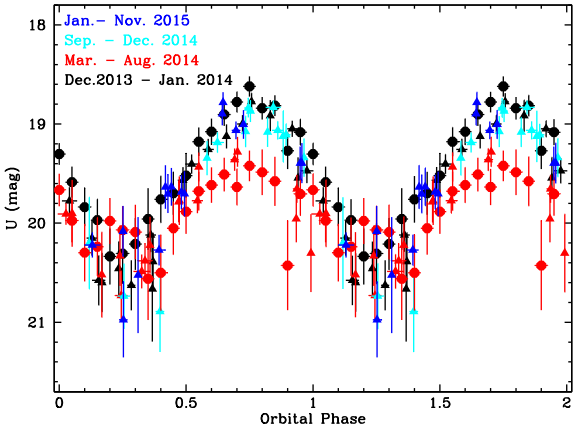

Figure 7. The *U*-band folded light curves of J1227 at the orbital period acquired by *Swift* UVOT from 2013 December to 2015 November (triangles) colour coded as 2013 December to 2014 January (black), 2014 March–August (red), 2014 September–December (cyan), and 2015 January–November (blue). The *XMM–Newton* OM (filled circles) light curves in 2013 December (black) and 2014 Junuary (red) (de Martino et al. 2015) are also reported for comparison. J1227 displays a lower amplitude modulation by a factor ∼2 as observed by both instruments only in the 2014 March–August period.

5 SPECTRAL ANALYSIS

The average 3–79 keV spectra from the *NuSTAR* FPMA and FPMB modules over the whole observation are featureless and of similar shape as those previously observed in the softer 0.3–10 keV range by Bogdanov et al. (2014), de Martino et al. (2015). The spectrum extends up to 70 keV without any apparent spectral break. An absorbed power-law model was adopted to fit the spectra with a multiplicative normalization constant to account for the differences of the FPMA and FPMB detectors, namely CONST*TBABS*POWERLAW in XSPEC.[10] However, since the hydrogen column density found from the *XMM–Newton* spectra in 2013 and 2014 (Bogdanov et al. 2014; de Martino et al. 2015) were both agreeing with an upper limit of $N_{\rm H} < 5 \times 10^{20}$ cm^{-2}, and due to the lack of sensitivity of the *NuSTAR* data to such low values, the hydrogen column density was fixed to zero. We then find a power-law photon index $\Gamma = 1.17 \pm 0.08$ (90 per cent confidence level) and an unabsorbed flux of $3.4 \pm 0.1 \times 10^{-12}$ erg cm^{-2} s^{-1} in the 3–79 keV range (see Table 5). The Γ-index is fully consistent with that we derived in the *XMM–Newton* data of 2013 December (1.07 ± 0.08) and 2014 June (1.2 ± 0.1). If a power law with an exponential cut-off is instead used, a worse fit is obtained ($\chi^2_{\rm red} = 1.13$, d.o.f. = 136) with a power-law photon index essentially the same, $\Gamma = 1.15 \pm 0.08$, and a cut-off energy >170 keV. The average flux in the 3–12 keV band is $4.7 \pm 0.3 \times 10^{-13}$ erg cm^{-2} s^{-1}, similar to that observed in 2013 December but lower than in 2014 June. With the above spectral parameters the X-ray luminosity in the 3–79 keV is $7.6^{+3.8}_{-0.8} \times 10^{32}$ erg s^{-1} for the adopted distance of $1.37^{+0.69}_{-0.15}$ kpc, accounting for the distance uncertainties.

To extend the spectral analysis into the soft energy range, *Swift* XRT (Burrows et al. 2005) data were then used. The monitoring of J1227 over the years encompasses observations performed in 2015, including April 25 (ObsId:81457001, 1.97 ks), but the short coverage results in a 0.3–10 keV spectrum with poor statistics. We then extracted XRT PC mode observations performed over a period of 4 months and with exposures longer than 1 ks, namely 2015 March 11 (ObsId:35101021, 2.78 ks), 2015 April 25, May 3 (ObsId:81457002 – 1.93 ks), 2015 June 22 (ObsId: 35101024, 2.22 ks), and 2015 July 3 (ObsId: 35101025), totalling 9.9 ks. The XRT PC mode data were extracted using the automatic analysis software (Evans et al. 2009) from the UK *Swift* Science Centre. During this period J1227 was found at an average count rate level (PC mode) of $\sim 5.7 \times 10^{-3}$ cts s^{-1}. The XRT 0.3–10 keV background subtracted light curve folded at the 6.91 h orbital period although with small gaps displays a minimum and a maximum at consistent phases as those observed in *XMM–Newton* and *NuSTAR* data but the fractional amplitude of the variability is poorly constrained (46±23 per cent), preventing a meaningful comparison. The accumulated XRT 0.3–10 keV spectrum grouped to have 5 counts per bin was fitted with an absorbed power law giving a photon index $\Gamma = 1.1^{+0.8}_{-0.4}$, an upper limit to the column density $N_{\rm H} < 2.4 \times 10^{21}$ cm^{-2}, and an unabsorbed flux of $3.6^{+0.9}_{-0.4} \times 10^{-13}$ erg cm^{-2} s^{-1}. When evaluated in the 3–6 keV range, the fluxes between *NuSTAR* and *Swift* agree within errors despite the uneven orbital coverage of the XRT instrument.

We then combined *Swift* and *NuSTAR* average spectra to perform a broad-band spectral fit (Fig. 8). Using the same model as before, leaving free the hydrogen column density of the absorber we obtain $N_{\rm H} < 1.2 \times 10^{21}$ cm^{-2} ($\chi^2_\nu = 1.0$, d.o.f. = 126) and all other parameters consistent with those without the addition of the *Swift* spectrum (Table 5). We then adopted a fixed hydrogen column

[9]Small-scale sensitivity patches in the UVOT detector are described at https://swift.gsfc.nasa.gov/analysis/uvot_digest/sss_check.html

[10]Details on XSPEC models available at https://heasarc.gsfc.nasa.gov/xanadu/xspec/manual/Models.html

Table 5. Spectral fit parameters of the *NuSTAR* spectra. Uncertainties are at the 90 per cent confidence level. The absorbing column density was set to 0 (see the text for details).

Parameter	Average	Orbital phase			
		$\Delta\Phi_{\rm min}$ 0.17–0.45	$\Delta\Phi_{\rm max}$ 0.69–0.99	$\Delta\Phi_{\rm rise}$ 0.45–0.69	$\Delta\Phi_{\rm decay}$ 0.00–0.17
$C_{\rm FPMB}$[a]	0.92 ± 0.07	$0.88^{+0.26}_{-0.25}$	$0.95^{+0.13}_{-0.11}$	$0.80^{+0.15}_{-0.13}$	$0.94^{+0.23}_{-0.19}$
Γ	1.17 ± 0.08	$1.13^{+0.27}_{-0.21}$	1.15 ± 0.13	$1.26^{+0.18}_{-0.17}$	$1.23^{+0.25}_{-0.24}$
Flux[b]	3.40 ± 0.10	$1.96^{+0.81}_{-0.59}$	$5.05^{+0.93}_{-0.81}$	$3.62^{+0.92}_{-0.76}$	$2.94^{+1.12}_{-0.84}$
χ^2_ν/d.o.f.	1.05/119	1.48/19	1.17/33	0.76/20	0.76/20

[a]Scaling constant for FPMB spectrum.
[b]Unabsorbed flux in units of 10^{-12} erg cm^{-2} s^{-1} in the 3–79 keV range.

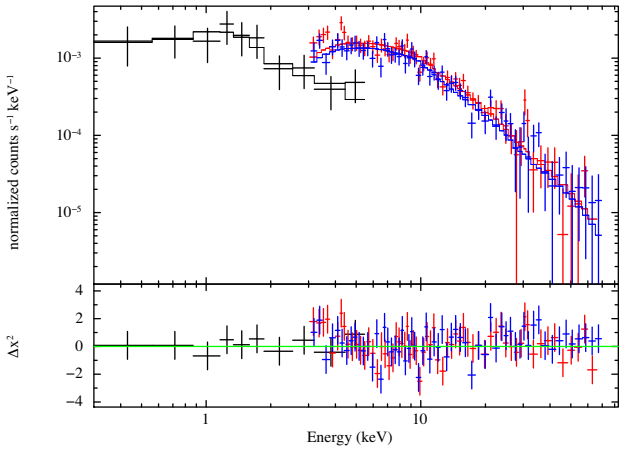

Figure 8. The average 2015 March–July *Swift* XRT (black) and 2015 April *NuSTAR* FPMA (red) and FPMB (blue) spectra fitted with an absorbed power-law model with $\Gamma = 1.17 \pm 0.08$, fixing $N_{\rm H} = 5 \times 10^{20}$ cm^{-2}.

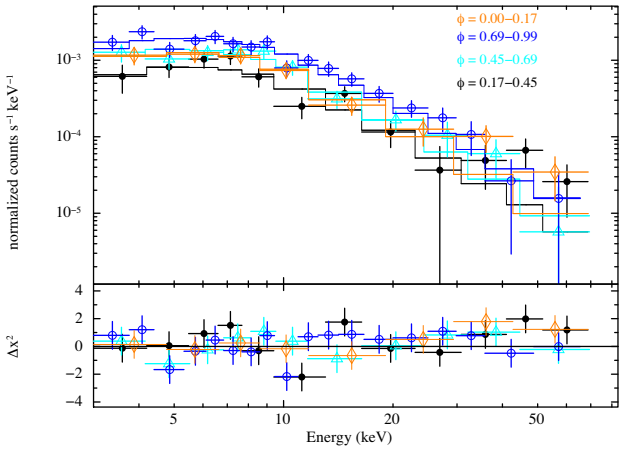

Figure 9. The phase-resolved *NuSTAR* spectra at orbital minimum (black filled points), maximum (blue empty circles), at rise to maximum (light blue empty triangles), and at decay to minimum (orange empty diamonds) are shown together with their best spectral model parameters reported in Table 5. For clarity purposes only the FPMB spectra are reported.

density to the value found with the *XMM–Newton* data. The total 0.3–79 keV unabsorbed flux is $3.7^{+0.2}_{-0.4} \times 10^{-12}$ erg cm^{-2} s^{-1}. This gives a luminosity of $8.3^{+4.2}_{-0.9} \times 10^{32}$ erg s^{-1} in the same energy range for $D = 1.37^{+0.69}_{-0.15}$ kpc.

Hints of changes in the spectral shape in the *XMM–Newton* data of 2013 December and 2014 June were found between the orbital maximum and minimum, with a tendency of a harder power-law index at maximum (Γ=1.1 $\pm$ 0.1) with respect to that at minimum ($\Gamma = 1.30^{+0.25}_{-0.15}$) (see de Martino et al. 2015). As seen in the hardness ratios in the selected energy ranges (Fig. 5), a tendency of a lower amplitude in the softer 0.3–3 keV band was found, but not at higher energies (see Section 4.1). This could produce a hardening of the spectrum at orbital maximum. The energy resolved *NuSTAR* orbital light curves also confirm the lack of energy dependence of the amplitudes above 3 keV and that the modulation is undetected above 25 keV. We however inspected the *NuSTAR* spectra along the orbital period by selecting four orbital phase ranges, namely the maximum ($\Delta\Phi_{\rm orb}$ = 0.69–0.99), the minimum ($\Delta\Phi_{\rm orb}$ = 0.17–0.45), the rise to maximum ($\Delta\Phi_{\rm orb}$ = 0.45–0.69), and the decay to the minimum ($\Delta\Phi_{\rm orb}$ = 0.0–0.17) (see Table 5). The variations essentially occur in the normalization with a power-law photon index being constant within uncertainties, although there is a tendency of a softer spectrum in the rise to and in the decay from maximum. The lack of orbital modulation above ∼25 keV is also apparent in the phase-resolved spectra (Fig. 9).

6 DISCUSSION

We here discuss the first X-ray data above 10 keV obtained with *NuSTAR* of the tMSP J1227 during the rotation-powered state complemented with a 2.5 yr-long radio coverage at *Parkes* telescope.

6.1 The radio monitoring

The radio monitoring spanning from 2014 June to 2017 February and carried mainly at 20 cm (1.4 GHz) provided us with a pulsar spin frequency at higher accuracy than previously reported (Roy et al. 2015) and a new orbital ephemeris, which is refined close to the 2015 April *NuSTAR* observation. The radio eclipses at 20 cm extend at least from $\Phi_{\rm orb} \sim 0.06$ to 0.39, although at some epochs the pulsar was not detected for a full orbital cycle. This gives a lower limit to the eclipse extent $\Delta\Phi_{\rm orb} \sim 0.3$. However at lower frequencies (e.g. 50 cm), the eclipse length could be as long as $\Delta\Phi_{\rm orb}$ ∼0.52–0.56 (Fig. 1). As a comparison, Roy et al. (2015) derive an eclipse length of $\Delta\Phi_{\rm orb} \sim 0.40$ at 607 MHz. Long eclipses up to 60 per cent of the orbital cycle are typical of RBs rather than BWs that instead have shorter eclipses (∼ 5–15 per cent). In both types of systems the eclipses are a signature of intrabinary material produced by the interaction of the pulsar and companion star winds likely in the form of a shock.

Using the thin-shell approximation for the collision of two isotropic winds (Canto, Raga & Wilkin 1996) and, for simplicity, that the shock axis of symmetry lies in the orbital plane (Romani & Sanchez 2016; Wadiasingh et al. 2017), the maximum shock opening angle as measured from the pulsar is related to the binary inclination and eclipse length through a simple trigonometric relation: $\cos\theta_{\rm max} = \sin {\rm i} \cos(\pi\ \Delta\Phi_{\rm orb})$. For J1227, assuming a very conservative lower limit to the radio eclipse length $\Delta\Phi_{\rm orb} \sim$0.4 and a binary inclination $46^\circ \lesssim i \lesssim 55^\circ$ (de Martino et al. 2015; Rivera Sandoval et al. 2018), the maximum shock opening angle would correspond to 75–77° or $\sim (5/12)\,\pi$. Following (Canto et al. 1996), the asymptotic shock angle is given by: $\theta_\infty - \tan\theta_\infty = \pi/(1-\eta^{-1})$, where $\eta = \dot{M}\, v_{\rm w}\, c/\dot{E}$ is the ratio of the secondary star to the pulsar wind momentum. The latter is related to the shock stagnation point radius, here from the MSP, as: $R_{\rm s}/a = \eta^{-1/2}/(1+\eta^{-1/2})$, where a is the binary separation (Canto et al. 1996). The estimated maximum shock opening angle would then give a maximum distance of the shock from the pulsar $(R_{\rm s}/a)_{\rm max} \sim 0.60$ and $\eta \sim 0.43$. Adopting the projected semimajor axis of the pulsar, $a1 = 0.668492$ lt-s (Table 2), the above binary inclination range and a mass ratio $q \sim 0.194$ (Roy et al. 2015), we obtain an orbital separation $a \sim 1.5{-}1.7 \times 10^{11}$ cm. Consequently, we estimate $R_{\rm s,max} \sim 0.6\,a \sim 1.0 \times 10^{11}$ cm, which is about the NS Roche lobe radius. However, in order to have the IBS formed around the pulsar, as indicated by the phasing of the X-ray light curves (see below), the condition $(R_{\rm s}/a)_{\rm max} \lesssim 0.50$ should be satisfied. The eclipse fraction observed at high frequencies then cannot provide a reliable estimate, but only a very loose lower limit to the eclipse fraction. In fact, RBs have longer eclipses at lower frequencies, with a dependence as $\sim \nu^{-0.4}$ (Broderick et al. 2016). As a comparison, for PSR J1023+0038 Wadiasingh et al. (2017) estimate $(R_{\rm s}/a)_{\rm max} \lesssim 0.4$ for an eclipse fraction $\gtrsim$0.6 at 350 MHz (Archibald et al. 2013). Our monitoring at *Parkes* encompasses only a few observations at 728 MHz and the previous measures by Roy et al. (2015) also had a few at 322 MHz. Scaling the eclipse length from 607 to 322 MHz, we derive $\Delta\Phi_{\rm orb} \sim 0.52$. Using instead this more likely value for the eclipse fraction, we obtain $(R_{\rm s}/a)_{\rm max} \sim 0.45$ and $\eta \sim 1.5$. As noted by Wadiasingh et al. (2017) caution should be taken in the direct interpretation of η in terms of wind ram pressure due to the gravitational influence of the pulsar. Additionally, the pulsar wind is likely to be more concentrated equatorially and an additional dependence of the MSP wind momentum as $\sin^n\theta_\star$ with $n \sim 2$, or even 4 for an oblique rotator, introduces changes in the shape of the IBS narrowing it at the poles (Romani & Sanchez 2016; Kandel et al. 2019).

6.2 The X-ray emission

The X-ray spectral shape is a power law with index of 1.2 with no spectral breakup to ∼70 keV, indicative of synchrotron cooling. The large orbital variability observed in J1227 and in other RBs, suggests that the IBS dominates the X-ray emission. This emission depends on the post-shock magnetic field strength (B_2) and on the ratio of magnetic to particle energy density σ (see Kennel & Coroniti 1984). In the case of weakly magnetized winds, σ could be as low as $\sim 3 \times 10^{-3}$ as in the Crab, while in strongly magnetized winds $\sigma \gg 1$. The post-shock magnetic field is related to the upstream magnetic field B_1 as $B_2 \sim 3\,B_1$ and $B_2 \sim B_1$ in these extreme cases, respectively (Kennel & Coroniti 1984). At large distances from the light cylinder that is for shock locations $R_{\rm s} >> R_{\rm LC}$, where $R_{\rm LC} = 8.1 \times 10^6$ cm is the radius of the light cylinder, the upstream magnetic field is given as $B_1 \sim [\sigma/(1+\sigma)]^{1/2}\,(\dot{E}/c\,f_{\rm p})^{1/2}\,R_{\rm s}^{-1}$, where $f_{\rm p}$ is the pulsar isotropic factor and $\dot{E}$ is the pulsar spin-down power (Arons & Tavani 1993). J1227 has a powerful pulsar with $\dot{E} \sim 9 \times 10^{34}$ erg s^{-1} and for $R_{\rm s} \lesssim R_{\rm max} \sim 0.45\,a = 7 \times 10^{10}$ cm and for an isotropic wind, $f_{\rm p} = 1$, we obtain $B_1 \gtrsim 1.4$ G for $\sigma = 3 \times 10^{-3}$ and $B_1 \gtrsim$ 20–25 G for high-σ wind conditions. Consequently, $B_2 \sim B_1 \gtrsim$ 20–25 G for $\sigma \gg 1$, whilst it is $B_2 \sim 3B_1 \gtrsim 4$ G for low-σ regimes. In both cases the magnetic field is large and higher than those in PWNe (Kennel & Coroniti 1984). These values are slightly larger than those derived by de Martino et al. (2015), who instead assumed the shock at the NS Roche lobe radius. The Lorentz factor of accelerated electrons is related to the maximum energy of synchrotron photons and post-shock magnetic field. The *NuSTAR* spectrum does not show a breakup to 70 keV and thus we conservatively assume $E_{x,\rm max}$ at this energy. Thus, $\gamma \sim 2.5 \times 10^5\,(E_{x,\rm max}/B_2)^{1/2} \sim$ (5–10) $\times 10^5$ for high and low magnetizations, respectively (Rybicki & Lightman 1979). The electron population has a power-law energy spectrum with index p related to the X-ray power-law index Γ as $p \sim 2\Gamma - 1 \sim 1.3$ below the maximum energy, extending at least down to ∼0.1–0.3 keV. Observations at lower energies only encompass FUV and UV bands with the shortest wavelength coverage at 2216 Å (Rivera Sandoval et al. 2018). At these wavelengths an excess of flux over the companion star emission has been detected primarily at orbital maximum and ascribed to the possible contribution of the IBS in the UV (Rivera Sandoval et al. 2018). However, the extrapolation of the synchrotron spectrum, using the derived power-law Γ index, gives a flux two orders of magnitude lower than that observed at 2216 Å. Here, we note that an additional bremsstrahlung component from an ADAF-like wind inflow contributing to the unmodulated flux has been recently suggested at soft X-ray energies, extending to UV and optical wavelengths (Wadiasingh et al. 2018), which could be possibly related to the observed UV excess. Hence, we can only set an upper limit of 0.1 keV to the synchrotron energy of the minimum Lorentz factor $\gamma_{\rm min}$, giving $\gamma_{\rm min} \lesssim 2{-}5 \times 10^4$. This range of high-$\gamma$ values implies a population of non-thermal emitting electrons from the shock in the X-ray domain. The hard p-index appears to contradict simple *Fermi*-type acceleration (diffusive shock acceleration) that predicts $p \sim$ 2.1–2.2 and could be in favour of magnetic dissipation (shock-driven magnetic reconnection) in the striped pulsar wind that predicts $p \sim$ 1–2 in high-σ regimes (see Sironi & Spitkovsky 2011a,b; Sironi, Keshet & Lemoine 2015).

The X-ray light curves of J1227 observed at different epochs all show a maximum at inferior conjunction of the pulsar $\phi_{\rm orb} \sim 0.75$. This phasing is observed in all RBs and it is opposite to what observed in BWs, which instead have a maximum at superior conjunction of the pulsar. The different behaviour is explained with a shock that wraps the pulsar in the RBs while the opposite occurs in BWs (Romani & Sanchez 2016; Wadiasingh et al. 2017). The light curves show different shapes over the years, with a broad asymmetric maximum in 2013 and 2015 centred at $\phi_{\rm orb} \sim 0.75$ but peaking around $\phi_{\rm orb}$ ∼0.7 and ∼0.9, respectively, with similar amplitudes. Instead, the modulation increases by a factor ∼2.2 in 2014 and has a well-defined double-peaked maximum, with peak separation $\Delta\Phi_{\rm orb} \sim 0.36$ and a dip reaching $\Delta I \sim 13$ per cent with respect to the maximum. If the shocked pulsar wind retains a moderately relativistic bulk motion, the synchrotron emission is expected to be Doppler boosted at inferior conjunction and de-boosted at superior conjunction of the NS, thus producing an X-ray orbital modulation (Arons & Tavani 1993; Dubus, Cerutti & Henri 2010; Dubus, Lamberts & Fromang 2015). The bulk Lorentz factor $\Gamma_{\rm L} = (1-\beta^2)^{-1/2}$ and bulk velocity $\beta = v/c$, drive the

Doppler boosting as $\delta_{\rm boost} = [\Gamma_{\rm L}(1 - \beta \cos\theta_{\rm v})]^{-1}$ where $\theta_{\rm v}$ is the viewing angle of the observer (Dubus et al. 2010). The synchrotron flux is expected to be enhanced by a factor $\delta_{\rm boost}^{2+({\rm p}-1)/2}$, along the orbit (Dubus et al. 2015) with a maximum to minimum flux ratio simplified as $\sim [(1 + \beta \sin i)/(1 - \beta \sin i)]^{2+(p-1)/2}$ (Dubus et al. 2010). The observed modulation amplitudes in 2013 and 2015, assuming $(p - 1)/2 = \Gamma_x = 1.2$ and binary inclination in the range 46–55° would then give $\beta \sim 0.2$ and $\Gamma_{\rm L} \sim 1.02$ while in 2014 $\beta \sim 0.3$ and $\Gamma_{\rm L} \sim 1.05$, indicating moderately relativistic bulk flow. A maximum flux enhancement of $\sim 2\,\Gamma_{\rm L,max}^{2+(p-1)/2}$ at the surface cap of the shock is predicted by the semi-analytical model of Wadiasingh et al. (2017) implying $\Gamma_{\rm L,max}$ ∼1.1 and ∼1.3 and $\beta_{\rm max} \sim 0.4$ and ∼0.7 in the observations of 2013/2015 and 2014, respectively. For moderately low binary inclinations as in J1227, broad maxima and weak amplitudes are predicted for low β values and small shock radii, while distinct double-peaked maxima and large amplitudes are expected for high bulk velocities and larger shock distances from the pulsar (Wadiasingh et al. 2017). The dip between the double-peaked maxima will have fractional intensities increasing at higher β and/or larger shock distances. Hence, the broad maximum observed in 2013 and 2015 indicates lower bulk velocities and smaller shock radii than those in 2014. Then, if the changes in the shape of the X-ray modulation are signatures of changes in the shock location, this may suggest that in 2013 and 2015 the donor star wind momentum was larger (smaller shock distance from the pulsar). Since optical modulation was stronger in 2013 and 2015 than in 2014 and anticorrelated with X-rays, it may be possible, as proposed in de Martino et al. (2015) that the shock had moved farther from the donor star at those two epochs, leaving more visible area of the heated face. The possibility that the companion Roche lobe filling factor could have changed, while appearing a viable explanation, would also imply a change in the optical flux at the orbital minimum, where the un-heated face of the secondary contributes. The *U*-band flux is however similar in all observations within uncertainties at this phase.

In addition, the light curves from soft to hard X-rays show a minimum skewed towards the rise to maximum. This is more evident in 2014 when the modulation is stronger and where the multisinusoidal fits require up to three harmonics. Although these are purely phenomenological descriptions, they may indicate that the structure of the IBS is asymmetric either due to Coriolis effects near the stagnation point (Wadiasingh et al. 2017) or at the shock boundaries (Wadiasingh et al. 2018). Consequently also the irradiation of the secondary star is expected to be asymmetric (Romani & Sanchez 2016; Kandel et al. 2019). The optical multicolour photometry of J1227 obtained in early 2015 indeed showed strong asymmetries in the portion of the light curves rising to the maximum (de Martino et al. 2015), supporting the possibility that an asymmetric shock may provide at least some of the heating.

Whether the shock is stable over years time-scale is still an unsolved matter since quasi-spherical radial infall on a pulsar is unstable on dynamical time-scales for distances outside the light cylinder (see Burderi et al. 2001). Recently (Wadiasingh et al. 2018) have investigated two possible mechanisms that could provide stability of a configuration where the shock is curved around the pulsar. One where the secondary star has a large dipole magnetic field of several kilogauss and low-mass-loss rates ($\lesssim 10^{15}\,{\rm g\,s^{-1}}$) and the other where instead the secondary mass-loss rate is large ($\sim 10^{15}$–$10^{16}\,{\rm g\,s^{-1}}$) with the flow in an ADAF-like configuration. However, both mechanism have their shortcomings (see details in Wadiasingh et al. 2018).

The lack of a detectable orbital modulation above 25 keV is unexpected result, not reported before for any of the other four RBs observed with *NuSTAR*, namely PSR J1023+0038 (Tendulkar et al. 2014), PSR J2129–0429 (Al Noori et al. 2018), PSR J1723–2837 (Kong et al. 2017), and PSR J2339–0533 (Kandel et al. 2019), although this could well depend on the choice of the energy bands used to study the X-ray modulations. Indeed, a more detailed study of the energy resolved X-ray orbital modulation in PSR J1023+0038 as observed with *NuSTAR* during its previous rotation-powered state reveals that above ∼25 keV the modulation has a fractional amplitude $\sim 15 \pm 3$ per cent, lower than that below 25 keV, $\sim 25 \pm 2$ per cent (1σ uncertainty) (Coti Zelati et al. in preparation). This smaller amplitude is consistent with the 3σ upper limit of ~ 10 per cent found in J1227. Small changes in the spectral shape between the minimum and maximum of the orbital modulation, although here undetected, could produce energy-dependent modulation amplitudes. For PSR J2339–0533, Kandel et al. (2019) find subtle changes in the phase-resolved X-ray spectra and a double-peaked light curve only below 15 keV, while between 15–40 keV it is single peaked. We here note that also for J1227, if studied over this wider energy range (e.g. 15–40 keV) the orbital modulation has about similar amplitude as in the softer *NuSTAR* bands. Indications of spectral changes along the double-peaked orbital modulation were also found in the *XMM–Newton* and *NuSTAR* data of PSR J2129–0429 (Al Noori et al. 2018). These would be the signature of different populations of cooling electrons whose spectrum is sensitive to the shape of the shock geometry and on the downstream magnetic field along the shock (Wadiasingh et al. 2017; Kandel et al. 2019). If the orbital modulation has a lower amplitude at high energies this may indicate that the electron population contributing to the shock emission at these energies has a different *p*-index or that a spectral break is hidden by the underlying magnetospheric pulsar emission. The latter has been successfully described by a magnetospheric synchrocurvature radiation model for the non-thermal γ and X-ray spectra of pulsars (Torres 2018; Torres et al. 2019) and would be dominant at minimum of the orbital modulation. The lack of detectable phase-resolved spectral variations above 3 keV (see Table 5) cannot help in discriminating the spectral shapes of the magnetospheric and IBS emissions. In fact even including two power-law components in the spectral fits and fixing the parameters of one to those found for the minimum we derive similar power-law indexes within errors and larger normalizations at the maximum, at the rise/decay to/from maximum.

For what concerns the softer X-ray band, i.e. 0.3–3 keV, as observed by *XMM–Newton* the modulation amplitude is lower than that at 3–6 keV by a factor of ∼1.4 in 2013 and 2014 (see Table 4). This would produce an overall hardening at orbital maximum or, vice versa a softer emission at orbital minimum and, indeed, a marginal change of the power-law index Γ from ∼1.1 to ∼1.3 between maximum and minimum was found (de Martino et al. 2015). Also in this case, an energy dependence of the X-ray light curve could be a signature of a spatial dependence along the shock of the electron *p*-index and thus less efficient (de-boosting) acceleration (Wadiasingh et al. 2017, 2018). However, the lack of spectral change and thus of energy-dependent modulation above 3 keV makes this hypothesis less viable. Alternatively, the softening at orbital minimum, i.e. at superior conjunction of the pulsar, below 3 keV could be explained by the additional contribution of the thermal emission of the NS where it is expected to be best visible. In de Martino et al. (2015) an upper limit of ~ 3 per cent of the

NS contribution to the average 0.3–10 keV flux was found, while at orbital minimum it is $\lesssim 40$ per cent. Although this does not allow a firm conclusion, it appears a viable interpretation. A future much longer exposure in the soft X-ray band may allow to put more stringent constraints on the NS thermal emission.

A strong irradiation (from ∼5500 to 6500 K) of the companion star in J1227 was found from optical spectroscopy and photometry, persistent in both rotation-powered and disc states (de Martino et al. 2014, 2015). Whether the late-type secondary is heated by the pulsar wind, by the X-ray emission from the IBS, or both could not be assessed due to the limited energy coverage of previous *XMM–Newton* observations. With the *NuSTAR* observation presented here, we derived an X-ray luminosity $L_x \sim 10^{33}$ erg s^{-1}, implying an efficiency $\eta_x = L_x/\dot{E} \sim 1$ per cent. The expected heating power impinging on to the companion star in the case of an isotropic pulsar wind is $L_{\rm heat,SD} = f_\Omega \dot{E}$, where f_Ω is the geometric factor $\sim 0.5\,(1-\cos\Omega)$ with $\Omega = a\tan(R_2/a)$, neglecting albedo. From optical photometry (de Martino et al. 2015), the secondary is found to fill its Roche lobe and thus $R_2/a = R_{L2}/a = 0.462\,(q/1+q)^{1/3}$, giving $f_\Omega \sim 0.01$ for q = 0.194. We then derive $L_{\rm heat,SD} \sim 9 \times 10^{32}$ erg s^{-1}. Similarly, if we consider the X-ray IBS emission located at $\sim 0.45\,a$ from the MSP, we obtain $L_{\rm heat,X} \sim 4 \times 10^{31}$ erg s^{-1}, which is only ∼ 4.4 per cent the expected heating from the pulsar spin-down power, and is only ∼ 3 per cent the luminosity of the irradiated face of the companion, $L_{\rm irr} = 4\,\pi\,R_2^2\,\sigma_{\rm SB}\,T_{\rm irr}^4 \sim 1$–$2 \times 10^{33}$ erg s^{-1} for $T_{\rm irr} \sim 6500$ K (de Martino et al. 2015).[11] Then the total irradiating luminosity, $L_{\rm heat,SD} + L_{\rm heat,X} \sim 10^{33}$ erg s^{-1}, is just about what necessary to heat the companion star. Different is the case where the shock power law extends into the MeV range (∼10 MeV), in which case the IBS alone would be energetically able to irradiate the secondary star. Alternatively the shock is located much closer (at) the companion but this would contrast with the geometry of the IBS wrapping the pulsar for the correct phasing of the orbital modulation.

We also note that additional heating could originate from shock particles that thread the companion magnetic field lines and are ducted to its surface (Sanchez & Romani 2017). Such possibility would require kilogauss magnetic field strengths for the secondary, hence a very active magnetic late-type star (large star-spots and/or flares) (Wadiasingh et al. 2018; Kandel et al. 2019). So far large star-spots are not identified in the optical light curves of RBs, although a few systems have been found to display flares (Romani et al. 2015; Deneva et al. 2016; Cho, Halpern & Bogdanov 2018). This additional heating has been invoked to explain asymmetries in the light curves of many RBs (Romani et al. 2015; Sanchez & Romani 2017). J1227 could also be affected by this mechanism.

7 CONCLUSIONS

We have presented the first *NuSTAR* hard X-ray data of the tMSP J1227 during its rotational-power state complemented with coordinated a 2.5 yr-long radio monitoring at *Parkes* telescope and with archival *XMM–Newton* and *Swift* data. Here, we summarize the main results:

(i) The *Parkes* monitoring gives us a refined orbital radio ephemeris around the *NuSTAR* observation, which we used to study the orbital dependent X-ray emission. The radio observations, mainly conducted at 1.4 GHz confirm the presence of long eclipses lasting ∼ 40 per cent of the orbit. The distance to J1227 derived from the DM is consistent with that obtained from *Gaia* DR2 parallax, $D = 1.37^{+0.69}_{-0.15}$ kpc.

(ii) The X-ray spectrum is non-thermal extending up to ∼70 keV without a spectral break and is consistent with a power law, with photon index $\Gamma = 1.17 \pm 0.08$. The X-ray emission is ascribed to an IBS formed between the pulsar and companion winds. We derive a luminosity in the 3–79 keV range of $7.6^{+3.8}_{-0.8} \times 10^{32}$ erg s^{-1}, using the *Gaia* distance.

(iii) The X-ray emission in the 3–79 keV range displays significant modulation at the 6.91 h orbital period with an amplitude of 28±3 per cent. Energy resolved orbital light curves show that the modulation is significantly detected below ∼25 keV with no energy dependence. Comparison with previous soft X-ray observations in the 0.3–12 keV with *XMM–Newton* reveals a mild softening only below 3 keV at superior conjunction of the NS. This suggests the possible contribution of the NS atmosphere to be confirmed with deeper soft X-ray observations than acquired so far.

(iv) We derive a 3σ upper limit to the modulation fraction above 25 keV of 10 per cent, which suggests that the electron population contributing to the shock emission at these energies is subject to different acceleration.

(v) The folded orbital light curves in common energy ranges as observed over three epochs by *NuSTAR* and *XMM–Newton* reveal changes in the amplitude over the years, indicating that the shock is not stationary and varies with time since J1227 transitioned into a rotation-powered state. We confirm previous finding of an anticorrelated variability between X-ray and optical ranges in the orbital modulation amplitudes.

(vi) We estimate for the shock luminosity in the 0.3–79 keV range $8.3^{+4.2}_{-0.9} \times 10^{32}$ erg s^{-1}, which is not enough alone to power the irradiation of the companion star unless the emission extends to the MeV range or the shock does not wrap the pulsar.

(vii) A search for X-ray pulses in the 3–79 keV range provides us with an upper limit to the rms pulse amplitude of 8.8 per cent, compatible with the upper limit derived in the 0.3–10 keV band from previous *XMM–Newton* data.

ACKNOWLEDGEMENTS

This work is based on observations obtained with the NASA science mission *NuSTAR*, with *XMM–Newton*, an ESA science mission with instruments and contributions directly funded by ESA Member States, with *Swift*, a NASA science mission with Italian participation, with *Parkes* telescope and with *Gaia*, an ESA mission. *Gaia* data are processed by the Data Processing and Analysis Consortium (DPAC). This work made use of data supplied by the UK *Swift* Science Data Centre at the University of Leicester. DdM, AP, and TMB acknowledge financial support from the Italian Space Agency (ASI) and National Institute for Astrophysics (INAF) under agreements ASI-INAF I/037/12/0 and ASI-INAF n.2017-14-H.0 and from INAF 'Sostegno alla ricerca scientifica main streams dell'INAF', Presidential Decree 43/2018. DdM, AP, MB, and AP also acknowledge support from INAF 'SKA/CTA projects', Presidential Decree 70/2016. DFT acknowledges support from the Spanish Ministry of Economy, Industry and Competitiveness grants PGC2018-095512-B-I00, SGR2017-1383, and AYA2017-92402-EXP. FCZ is supported by a Juan de la Cierva fellowship and grants from the Spanish Ministry of Economy, Industry and

[11] The effect of irradiation is to suppress the temperature gradient in the outer stellar envelope, blocking the outwards transport of energy through the face. A detailed rigorous treatment of irradiation can be found in Ritter, Zhang & Kolb (2000).

Cometitiveness grants SGR2017-1383 and PGC2018-095512-B-I00. We also thank the 'PHAROS' COST Action (CA16214) for partial support. We also acknowledge useful discussion with Dr. A. Sanna on the *NuSTAR* data timing analysis.

REFERENCES

Al Noori H. et al., 2018, ApJ, 861, 89
Alpar M. A., Cheng A. F., Ruderman M. A., Shaham J., 1982, Nature, 300, 728
Ambrosino F. et al., 2017, Nat. Astron., 1, 854
Archibald A. M. et al., 2009, Science, 324, 1411
Archibald A. M., Kaspi V. M., Bogdanov S., Hessels J. W. T., Stairs I. H., Ransom S. M., McLaughlin M. A., 2010, ApJ, 722, 88
Archibald A. M., Kaspi V. M., Hessels J. W. T., Stappers B., Janssen G., Lyne A., 2013, preprint (arXiv:1311.5161)
Archibald A. M. et al., 2015, ApJ, 807, 62
Arons J., Tavani M., 1993, ApJ, 403, 249
Backer D. C., Kulkarni S. R., Heiles C., Davis M. M., Goss W. M., 1982, Nature, 300, 615
Bailer-Jones C. A. L., Rybizki J., Fouesneau M., Mantelet G., Andrae R., 2018, AJ, 156, 58
Bassa C. G. et al., 2014, MNRAS, 441, 1825
Bellm E. C. et al., 2016, ApJ, 816, 74
Bogdanov S., Patruno A., Archibald A. M., Bassa C., Hessels J. W. T., Janssen G. H., Stappers B. W., 2014, ApJ, 789, 40
Bogdanov S. et al., 2015, ApJ, 806, 148
Bogdanov S. et al., 2018, ApJ, 856, 54
Broderick J. W. et al., 2016, MNRAS, 459, 2681
Burderi L. et al., 2001, ApJ, 560, L71
Burrows D. N. et al., 2005, Space Sci. Rev., 120, 165
Campana S., Di Salvo T., 2018, in Rezzolla L., Pizzochero P., Jones D. I., Rea N., Vidaña I., eds, Astrophysics and Space Science Library, Vol. 457, The Physics and Astrophysics of Neutron Stars. Springer, Berlin, p. 149
Campana S., Miraval Zanon A., Coti Zelati F., Torres D. F., Baglio M. C., Papitto A., 2019, A&A, 629, L8
Canto J., Raga A. C., Wilkin F. P., 1996, ApJ, 469, 729
Cho P. B., Halpern J. P., Bogdanov S., 2018, ApJ, 866, 71
Cordes J. M., Lazio T. J. W., 2002, preprint (arXiv:astro-ph/0207156)
Coti Zelati F. et al., 2014, MNRAS, 444, 1783
D'Angelo C. R., Spruit H. C., 2012, MNRAS, 420, 416
de Martino D. et al., 2010, A&A, 515, A25
de Martino D. et al., 2013, A&A, 550, A89
de Martino D. et al., 2014, MNRAS, 444, 3004
de Martino D. et al., 2015, MNRAS, 454, 2190
Deneva J. S. et al., 2016, ApJ, 823, 105
Dubus G., Cerutti B., Henri G., 2010, A&A, 516, A18
Dubus G., Lamberts A., Fromang S., 2015, A&A, 581, A27
Ertan Ü., 2017, MNRAS, 466, 175
Evans P. A. et al., 2009, MNRAS, 397, 1177
Ferrigno C. et al., 2014, A&A, 567, A77
Gaia Collaboration, 2018, A&A, 616, A1
Harrison F. A. et al., 2013, ApJ, 770, 103
Hobbs G. B., Edwards R. T., Manchester R. N., 2006, MNRAS, 369, 655
Hui C. Y. et al., 2015, ApJ, 801, L27
Jennings R. J., Kaplan D. L., Chatterjee S., Cordes J. M., Deller A. T., 2018, ApJ, 864, 26
Johnson T. J. et al., 2014, ApJS, 213, 6
Johnson T. J. et al., 2015, ApJ, 806, 91
Kandel D., Romani R. W., An H., 2019, ApJ, 879, 73
Keith M. J. et al., 2010, MNRAS, 409, 619
Kennel C. F., Coroniti F. V., 1984, ApJ, 283, 710
Kong A. K. H., Hui C. Y., Takata J., Li K. L., Tam P. H. T., 2017, ApJ, 839, 130
Leahy D. A., 1987, A&A, 180, 275
Linares M., 2014, ApJ, 795, 72
Lindegren L. et al., 2018, A&A, 616, A2
Lorimer D., Kramer M., 2005, The Observatory, 125, 338
Lorimer D. R. et al., 2006, MNRAS, 372, 777
Papitto A., Torres D. F., 2015, ApJ, 807, 33
Papitto A. et al., 2013, Nature, 501, 517
Papitto A., Torres D. F., Rea N., Tauris T. M., 2014, A&A, 566, A64
Papitto A., de Martino D., Belloni T. M., Burgay M., Pellizzoni A., Possenti A., Torres D. F., 2015, MNRAS, 449, L26
Papitto A. et al., 2019, ApJ, 882, 104
Patruno A. et al., 2014, ApJ, 781, L3
Ritter H., Zhang Z.-Y., Kolb U., 2000, A&A, 360, 969
Rivera Sandoval L. E. et al., 2018, MNRAS, 476, 1086
Roberts M. S. E., McLaughlin M. A., Gentile P. A., Ray P. S., Ransom S. M., Hessels J. W. T., 2015, preprint (arXiv:1502.07208)
Roberts M. S. E. et al., 2018, in Weltevrede P., Perera B. B. P., Preston L. L., Sanidas S., eds, IAU Symp. Vol. 337, Pulsar Astrophysics the Next Fifty Years. Cambridge Univ. Press, Cambridge, p. 43
Romani R. W., Sanchez N., 2016, ApJ, 828, 7
Romani R. W., Graham M. L., Filippenko A. V., Kerr M., 2015, ApJ, 809, L10
Roming P. W. A. et al., 2005, Space Sci. Rev., 120, 95
Roy J. et al., 2015, ApJ, 800, L12
Rybicki G. B., Lightman A. P., 1979, Radiative Processes in Astrophysics. Wiley-Interscience, New York
Sanchez N., Romani R. W., 2017, ApJ, 845, 42
Sanna A. et al., 2017, MNRAS, 466, 2910
Sironi L., Spitkovsky A., 2011a, ApJ, 726, 75
Sironi L., Spitkovsky A., 2011b, ApJ, 741, 39
Sironi L., Keshet U., Lemoine M., 2015, Space Sci. Rev., 191, 519
Standish E. M., 1998, A&A, 336, 381
Stappers B. W. et al., 2014, ApJ, 790, 39
Staveley-Smith L. et al., 1996, Publ. Astron. Soc. Aust., 13, 243
Strader J. et al., 2019, ApJ, 872, 42
Takata J. et al., 2014, ApJ, 785, 131
Tendulkar S. P. et al., 2014, ApJ, 791, 77
Thorstensen J. R., Armstrong E., 2005, AJ, 130, 759
Torres D. F., 2018, Nat. Astron., 2, 247
Torres D. F., Ji L., Li J., Papitto A., Rea N., de Oña Wilhelmi E., Zhang S., 2017, ApJ, 836, 68
Torres D. F., Viganò D., Coti Zelati F., Li J., 2019, MNRAS, 489, 5494
Turner M. J. L. et al., 2001, A&A, 365, L27
Vaughan B. A. et al., 1994, ApJ, 435, 362
Veledina A., Nättilä J., Beloborodov A. M., 2019, ApJ, 884, 144
Venter C., Johnson T. J., Harding A. K., 2012, ApJ, 744, 34
Wadiasingh Z., Harding A. K., Venter C., Böttcher M., Baring M. G., 2017, ApJ, 839, 80
Wadiasingh Z., Venter C., Harding A. K., Böttcher M., Kilian P., 2018, ApJ, 869, 120
Yao J. M., Manchester R. N., Wang N., 2017, ApJ, 835, 29

This paper has been typeset from a TEX/LATEX file prepared by the author.